

# Using spacer layers to control metal and semiconductor absorption in ultrathin solar cells with plasmonic substrates

Niraj N. Lal,<sup>1</sup> Hang Zhou,<sup>2</sup> Matthew Hawkey,<sup>1</sup> Jatin K. Sinha,<sup>3</sup> Philip N. Bartlett,<sup>3</sup>  
Gehan A. J. Amaratunga,<sup>2</sup> and Jeremy J. Baumberg<sup>1</sup>

<sup>1</sup>*NanoPhotonics Center, Cavendish Laboratory, University of Cambridge, Cambridge CB3 0HE, United Kingdom*

<sup>2</sup>*Centre for Advanced Photonics and Engineering, University of Cambridge CB3 0HE, United Kingdom*

<sup>3</sup>*School of Chemistry, University of Southampton SO17 1BJ, United Kingdom*

(Received 24 March 2012; revised manuscript received 24 May 2012; published 25 June 2012)

We systematically explore the performance of ultrathin amorphous silicon solar cells integrated on plasmonic substrates of several different morphologies. Angle-resolved reflectance, external quantum efficiency measurements, and finite-difference time-domain simulations highlight the importance of the spacer layer in determining the mode profiles to which light can couple. Coupling mechanisms are found to strongly differ between periodic silver nanovoid arrays and randomly textured silver substrates. Tailoring the spacer thickness leads to 50% higher quantum efficiencies and short-circuit current densities by tuning the coupling between the near-field and trapped modes with enhanced optical path lengths. The balance of absorption for the plasmonic near field at the metal/semiconductor interface is analytically derived for a broad range of leading photovoltaic materials. This yields key design principles for plasmonic thin-film solar cells, predicting strong near-field enhancement only for CdTe, CuInGaSe<sub>2</sub>, and organic polymer devices.

DOI: [10.1103/PhysRevB.85.245318](https://doi.org/10.1103/PhysRevB.85.245318)

PACS number(s): 78.20.Jq, 72.40.+w, 73.20.Mf

## I. INTRODUCTION

Thin solar cells are promising candidates for wide-scale low-cost sustainable electricity generation. Thin films use less semiconductor material (often costly and/or rare), have higher manufacturing throughput, and enhanced electrical performance due to the increased electric field within the device. For amorphous silicon, the increased field reduces the photodegradation commonly observed for thick cells. Shorter cell thicknesses also allow the use of novel materials as absorbing layers. Opposing the deployment of thinner cells is the need for large optical thicknesses to efficiently harvest the full solar spectrum. Broadband absorption within thin devices requires the careful design of optical feature geometry within each cell.

Over the past decade the plasmonic response of nanostructured noble metals has been utilized to enhance absorption in various thin film devices. Several light-trapping geometries have been explored<sup>1,2</sup> including those based on nanoparticles,<sup>3</sup> nanocavities,<sup>4-7</sup> nanoholes,<sup>8-10</sup> gratings,<sup>11-13</sup> and dome nanotextures.<sup>14-16</sup> Research to date has mainly focused on scatterer topography, order, and structural periodicity of these metallic features, showing that the enhancement of cell efficiency is possible with careful optimization. Recent reviews describe the promising potential for plasmonics in ultrathin solar cells through coupling to guided modes within devices.<sup>17</sup>

Here we present ultrathin amorphous silicon solar cells fabricated on three different substrate geometries: sphere-segment nanovoids, silver-coated randomly textured glass, and flat silver. We also explore a key parameter on which light coupling is found to sensitively depend: that of the spacer layer. This layer is often included in solar cell devices as a transparent conducting spacer between the rear-reflector and active semiconductor. Its role is to prevent the diffusion of the metal into the semiconductor, enhance reflection from the rear surface, act as a selective electron/hole-transporter, or a mix of all of the above. For a-Si:H solar cells fabricated on silver contacts, a spacer layer is necessary to prevent

the diffusion of metal into the semiconductor. Research on the dielectric layer between the plasmonic feature and active absorber has examined the distance dependence of thin crystalline Si solar cells separated by a dielectric from silver nanoparticles,<sup>18,19</sup> the decrease in absorption enhancement of the active absorber in dye-sensitized cells separated by titania from plasmonic nanoparticles,<sup>20</sup> and the ability of the near field of plasmonic particles to enhance absorption in ultrathin semiconductors.<sup>21</sup> With plasmonic substrates, previous research has investigated the optical response of a-Si:H solar cells with plasmonic gratings,<sup>22,23</sup> numerically simulated the dependence of buffer thickness on waveguide modes,<sup>24-26</sup> and examined the buffer layer effect on performance for randomly textured reflectors for thick a-Si solar cells.<sup>27</sup> In this article we combine optical measurements, electrical characterization, and finite-difference time-domain (FDTD) simulations of ultrathin amorphous silicon solar cells with different plasmonic substrates and spacer layer thicknesses, and identify key design principles for solar cells built from leading contenders of thin film materials. The study of thin solar cells, with only 50 nm of a-Si:H active layer, provides detailed access to understanding the absorption-enhancing properties of the underlying nanostructures.

Device performance can be understood in terms of Fermi's golden rule; by adjusting the local density of states to which light can couple, the absorption enhancement in the active semiconductor layer can be optimized, allowing an increase of up to 50% in efficiency and short-circuit current density. The spacer layer is found to sensitively mediate the coupling of light to plasmonic near-field excitations and guided modes within the plane, allowing a further tool for optimizing absorption enhancement.

Section II introduces the fabrication of devices with three substrate geometries: flat, hemi-spherical nanovoids, and randomly textured glass (Fig. 1). Section III examines angularly resolved reflectance for each geometry and presents short-circuit current density dependencies on spacer layer

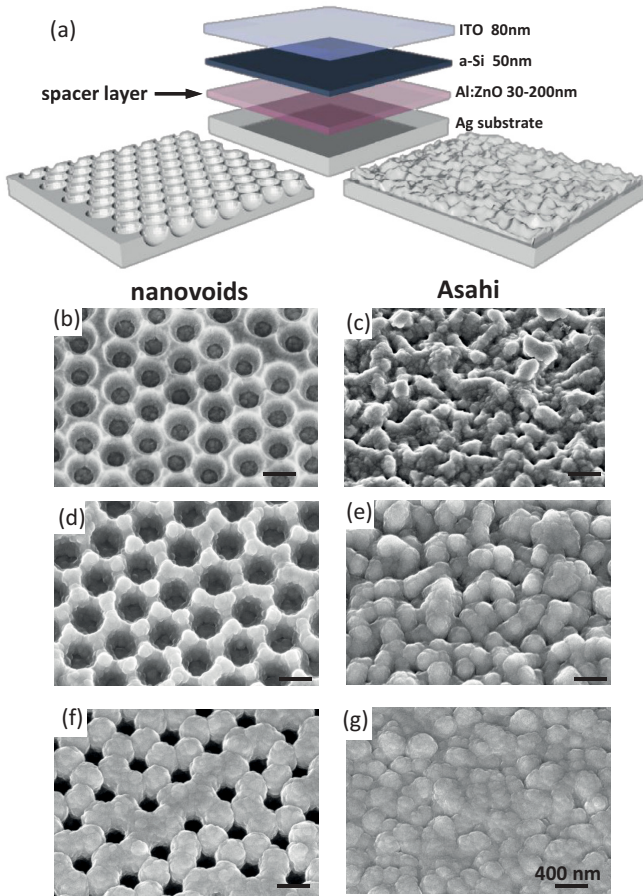


FIG. 1. (Color online) (a) Schematic representation of substrate and layer structure. (b, c) Scanning electron micrographs of silver nanovoids (radius 250 nm) and silver-coated Asahi glass. Nanovoids and Asahi glass coated with (d, e) 30 and (f, g) 200 nm of Al:ZnO and 50 nm a-Si.

thickness. Section IV discusses the optical physics within each device and the guided-mode coupling dependence on roughness, and Sec. V analytically derives and explores the balance of absorption between the underlying plasmonic substrate and the active semiconductor layers for commonly used solar cell materials.

## II. METHODS

Three substrate geometries are investigated as the Ag back contact of ultrathin a-Si solar cells: sphere-segment silver nanovoids of radius 100–250 nm grown to half-height, silver-coated randomly textured glass (150 nm Ag thermally evaporated onto Asahi VU-type<sup>28</sup>), and flat cells (Fig. 1), each providing a framework for the investigation of different light-coupling mechanisms within the ultrathin solar cell. Flat cells serve as the reference for scattering-unassisted absorption within the device, with the support of standing-wave Fabry-Perot (FP) type modes for thicker cell layers. Sphere-segment nanovoids harness strong plasmonic resonances weakly tethered to the metal surface<sup>29,30</sup> allowing the tracking of plasmonic mode shifts with different material coatings. Asahi VU type glass is a commercially available glass with known roughness and serves as a quantitative,

reproducible representative of a randomly textured plasmonic substrate. Silver nanovoids are grown via self-assembly and subsequent electrochemical deposition, while Asahi VU type glass and flat glass substrates are treated with 10 nm Cr and 150 nm Ag via thermal evaporation. Each substrate is coated with zinc oxide–aluminium oxide (99-1% wt, Testbourne Ltd.) via RF magnetron sputtering to thicknesses of  $\delta_{AZO} = 30, 100, \text{ and } 200$  nm, overcoated with 50 nm of a-Si:H (15 nm *n* type, 35 nm *i* type) via plasma-enhanced chemical vapor deposition (RF Plasmalab  $\mu$ P), before RF sputtering 80 nm of indium tin oxide (ITO) as the top contact. These materials deposit conformably with the gradual smoothing of features with increased layer thickness (Fig. 1). External quantum efficiency (EQE) measurements are performed using a 250 W tungsten halogen lamp (Newport, Simplicity QTH) dispersed through a monochromator (Oriel Cornerstone 130) used with a filter wheel to block higher spectral orders. Illumination is at normal incidence; the angular absorption dependence is extracted via the goniometer measurements discussed below. Current is measured with a Keithley 2635 source measure unit. Short-circuit current density measurements are obtained via integrating the external quantum efficiency response:  $J_{sc} = \int N(\lambda) \times EQE(\lambda) d\lambda$ , with  $N(\lambda)$  the photon flux of the AM 1.5 G spectrum.  $J_{sc}$  measurements are further separated for wavelengths above and below 600 nm to elucidate detail from short and near band-gap edge regions of the spectrum. Full EQE spectra for each device are included in the Appendices.

## III. GEOMETRY

### A. Nanovoids

Nanovoids possess distinct plasmonic resonances that resonate as anti-nanoparticle-like modes within the cavity. Through Mie theory we are able to identify resonances associated with defined angular momentum values in angle-resolved reflectance scans<sup>30</sup> [Fig. 2(a)]. Nanovoids with a 250-nm radius are presented in this section, with the results of varying radii presented in Sec. IV C. Reflectance measurements are taken using a supercontinuum white-light laser (Fianium) with wavelength range 410–1500 nm, and are normalized to flat silver. Light is of transverse magnetic (TM) polarization (transverse electric (TE) data are included in the Appendices). Plotting energy versus angle provides direct access to the energy-momentum dispersion relation of the optical resonances.

With a 30-nm coating of aluminium-doped zinc oxide (Al:ZnO), the plasmonic resonances redshift due to the higher refractive index compared to air [Fig. 2(c)]. These resonances retain sharp linewidths and high intensities indicating strong confinement and long plasmon lifetimes which prove significant in the contribution to active semiconductor absorption in the a-Si coated device, discussed further below. Higher-order modes tune into the visible spectrum for 200 nm of Al:ZnO coating [Fig. 2(d)] alongside interaction with standing-wave modes within the curved Al:ZnO cavity.

Optical absorption modes of nanovoids coated with the complete cell structure of Al:ZnO/a-Si/ITO exhibit strong dependence on the thickness of the spacer layer. Bragg-scattering-like surface plasmon modes [black lines in Fig. 2(e)] alongside photonic-crystal-like modes (white lines) arising

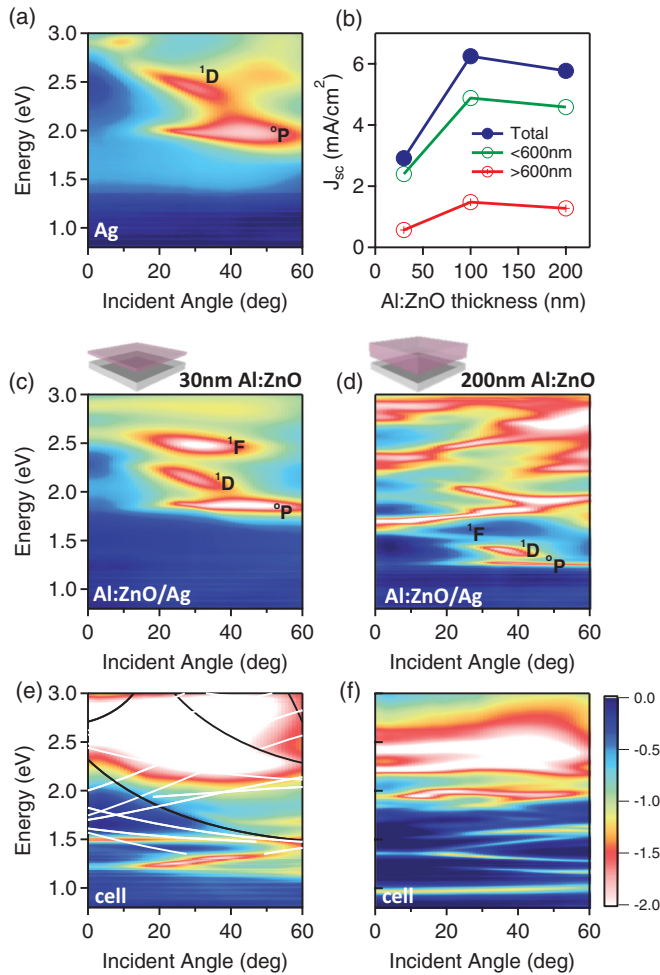


FIG. 2. (Color online) Angle reflectance scans of silver nanovoids (250-nm radius) (a) uncoated, (c, d) coated with Al:ZnO of 30 and 200 nm, (e, f) and complete solar cells as indicated. Color scale is  $\log(\text{reflectance})$  with blue indicating high reflectance and red-white indicating low reflectance. Modes labeled according to Ref. 30. (b) Short-circuit current density for nanovoids cells versus Al:ZnO thickness, decomposed for  $\lambda < 600$  nm and  $\lambda > 600$  nm.

from the hexagonal lattice of nanovoids are present in the solar cell with a thin Al:ZnO coating.<sup>29</sup> Strong extinction is observed for energies  $> 2.3$  eV owing to both scattering from the structure and absorption in the metal layer. For solar cells with a thick Al:ZnO coating the absorption is dominated by nondispersive localized plasmon modes within the voids structure [Fig. 2(f)], where the broad spread of each mode in a wave vector (angle) shows localization in real space.

These optical interactions within the device manifest in the electrical response of the solar cells [Fig. 2(b)]. Whereas optical extinction includes scattering, parasitic absorption in the metal and photocurrent generated in the active semiconductor, spectrally resolved *electrical* measurements highlight the optical modes that contribute to enhanced efficiency.

Parasitic absorption in the silver substrate for 30-nm Al:ZnO coated cells is reduced once the Al:ZnO spacer thickness increases to 100 nm, in agreement with measurements on thin Ag gratings,<sup>22</sup> causing the sharp doubling of  $J_{sc}$  from 3 to 6  $\text{mAcm}^{-2}$ . The enhancement is primarily produced

at shorter wavelengths where the tightly confined localized surface plasmon resonances (LSPRs) is allowed to occupy more of the nanovoid cavity with an increasing spacer layer. The vertical surface plasmon decay length for a flat Ag/Al:ZnO interface  $[|k_z|^{-1}]$  where  $k_z = \sqrt{k_{||}^2 - \epsilon_{AZO}(\frac{\omega}{c})^2}$  is 90 nm for light of 600-nm wavelength and hence, for the 30-nm Al:ZnO coated cell, the plasmon mode still strongly overlaps with the a-Si layer.  $k_{||}$  here is the surface plasmon wave vector and  $\epsilon_{AZO}$  is the dielectric function for Al:ZnO. For amorphous silicon this overlap leads to significant absorption in the silver layer and hence suppressed photocurrent at shorter wavelengths, further discussed in Sec. V.

We find the main effect of localized plasmons in silver nanovoids with 30 nm of spacer layer to be quenching of optical modes leading to absorption in the metal. With 100 nm of the Al:ZnO spacer layer, the optical thickness of the entire device, now  $> 560$  nm, is able to support modes that are a mix between localized plasmons and standing-wave modes within the cavity. The good overlap of this field profile with the active semiconductor layer contributes to the strong increase in  $J_{sc}$ . With 200 nm of Al:ZnO, less absorption is present between 1.5–2 eV and above 2.5 eV [Fig. 2(f)]. This decrease in the overlap of the optical mode with the absorption spectrum of the a-Si layer especially for shorter wavelengths is responsible for the slight decrease in photocurrent within the device.

## B. Randomly textured

Silver-coated randomly textured glass displays the broad plasmonic resonances expected from an agglomeration of silver nanoparticles of assorted size between 50–200 nm [Fig. 3(a)]. The resonances redshift from the quasistatic dipole peak for silver nanoparticles at 400 nm (3.1 eV), and broaden when coated with 30 nm of Al:ZnO [Fig. 3(c)] due to its higher refractive index. When coated with a-Si and ITO layers, the 30 nm Al:ZnO cell shows further redshifts and broadening of the localized resonances along with absorption from the a-Si layer [Fig. 3(e)]. For the textured silver coated with 200 nm of Al:ZnO a distinctly different reflectance response is observed with strong extinction at Fabry-Perot (FP) resonance  $\lambda = 2n\delta_{AZO}$  [Fig. 3(d)]. When coated with cell layers [Fig. 3(f)] this increased optical thickness enables the plasmonic resonances of the textured silver to resonantly scatter light in-plane within the device. The longer optical path lengths arising from this scattering accounts for the difference between the Asahi and flat cells, discussed further in Sec. III C.

These optical features again manifest in the electrical response of each cell. For the 30-nm Al:ZnO cell, localized surface plasmon resonances (LSPRs) arising at the tips and cavities of the textured silver substrate generate absorption in the silver layer, suppressing the photocurrent for shorter wavelengths similarly as for the nanovoid solar cell. As the spacer thickness increases to 100 nm and the silicon layer spatially moves away from the strong near field at the Ag/Al:ZnO interface, the increased optical thickness now supports scattering in-plane generating enhanced absorption across the spectrum and contributing to a 30% increase in photocurrent from 5.2–6.7  $\text{mAcm}^{-2}$ .

With 200 nm of Al:ZnO further enhancement to scattered optical path lengths is supported, with field profiles that overlap

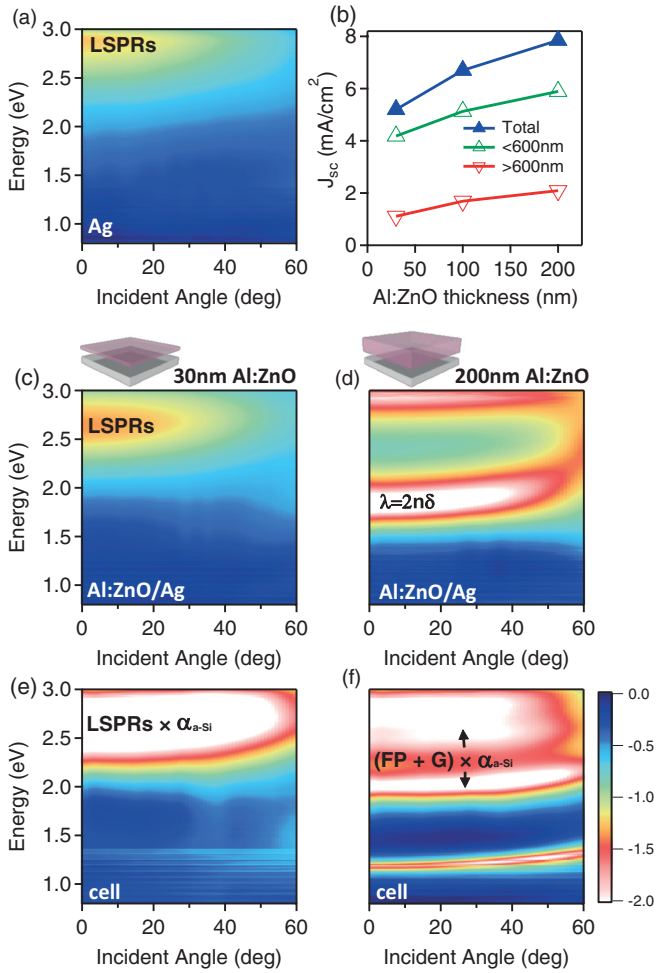


FIG. 3. (Color online) Angularly resolved reflectance for (a) silver-coated randomly textured glass, (b, c) coated with Al:ZnO and (d, e) complete cell layers. (f) Photocurrent measurements with varying Al:ZnO thickness. Labelling discussed in text.

with the a-Si layer both spatially and spectrally at  $\sim 2$  eV, as shown with finite-difference time-domain simulations in Sec. IV A. This field profile generates increased photocurrent within the device [Fig. 3(b)] to 7.9 mA/cm<sup>2</sup>, 50% higher than for the 30-nm device. This electrical response is due to both the broad scattering resonance of the silver-coated textured glass embedded within the FP-type cavity profile, alongside the enhanced optical thickness within the device supporting multiple guided (G) modes. The scattering contribution of the textured dielectric layer interface is also significant and has been shown to provide strong enhancement to optical path length and absorption for both random and periodic structures.<sup>31</sup> We examine here the contribution of the plasmonic Ag back reflector in concert with the textured Al:ZnO–a-Si:H interface.

This sensitive dependence to total optical thickness becomes apparent with ultrathin absorbing layers. Previous research has examined cells with active material thicknesses larger than that required to absorb most of the incident light.<sup>15,22,27</sup> Here, with approximately a quarter of the natural absorption thickness we are able to enhance photocurrent by 50% compared to devices with 30 nm of Al:ZnO, by increasing only the spacer layer thickness. A key optical design feature

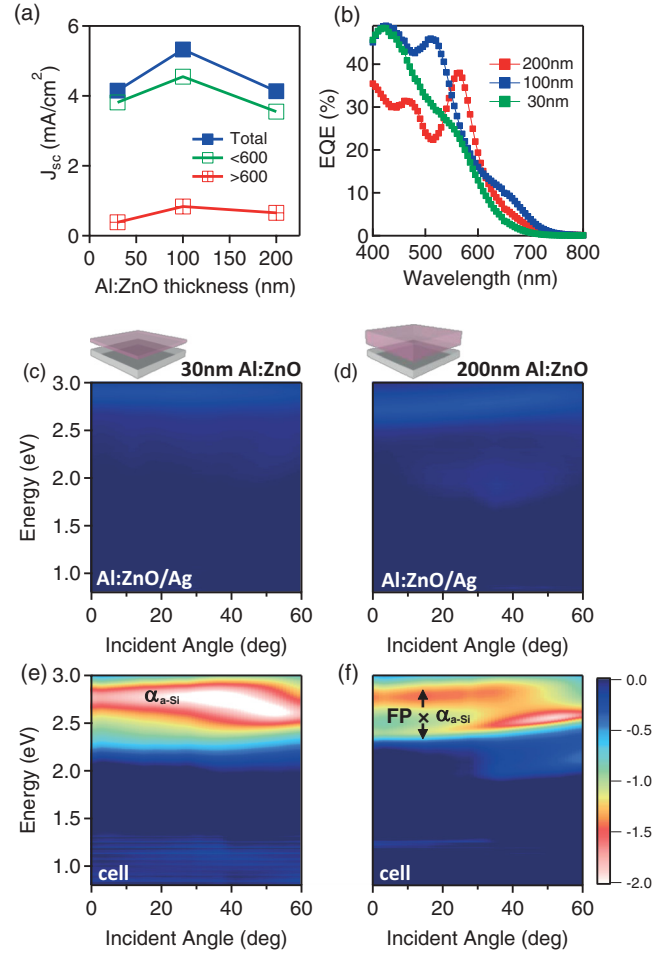


FIG. 4. (Color online) (a) Short-circuit current density and (f) EQE measurements for flat cells with changing Al:ZnO thickness. Angle-resolved reflectance of Al:ZnO (b, c) coated silver (d, e) and with additional solar cell layers.

for ultrathin solar cells is identified that significant absorption gains can be made through the inclusion of optically thick spacer layers, without the need for increasing semiconductor thickness. These results bridge those from thin solar cells on plasmonic substrates and those based on waveguide architectures with nonabsorbing cladding layers.<sup>32</sup>

### C. Flat

While a practical reference architecture for industry is solar cells fabricated on randomly textured metal, cells fabricated on flat silver provide a baseline for device performance unassisted by both plasmon near-field and enhanced scattering. As expected, angle-resolved reflectance of flat silver coated with 30 nm of Al:ZnO [Fig. 4(c)] shows little change from flat silver, with the 200-nm coated silver [Fig. 4(d)] showing the faint onset of Fabry-Perot (FP) resonance at 2.6 eV.

The spectral overlap of the FP resonance with the absorption spectrum of a-Si proves important for producing sufficient absorption in the ultrathin a-Si layer. The strong absorption at 2.7 eV (460 nm) due to the FP resonance at short wavelengths [Fig. 4(e)] for the 30-nm coated cell is the reason for the major contribution to  $J_{sc}$  of light with  $\lambda < 600$  nm [Fig. 4(a)]. As the

spacer layer thickness increases to 100 nm, the FP resonance peak shifts spectrally towards the red while spatially being now located inside the a-Si layer (see Sec. IV A), contributing to a 25% increase in photocurrent from 4.2–5.3 mA/cm<sup>2</sup>. From EQE measurements [Fig. 4(b)] we see the spectral position of the FP peak redshifts out of the region of strong absorption from a-Si:H at shorter wavelengths. Alongside the spectral overlap, for ultrathin cells, the *spatial* overlap of the field profile with the absorbing layer proves important, and we observe this via FDTD simulation discussed below.

#### IV. DISCUSSION

##### A. Simulations

We find the role of the spacer layer to vary for each cell geometry. FDTD simulations<sup>33</sup> highlight the changing field profiles across each device with changing spacer thicknesses (Fig. 5). Simulations are in three dimensions (3D), dielectric constants for Ag (Ref. 34), Al:ZnO (Ref. 35), a-Si:H (Ref. 36), and ITO (Ref. 36) are taken from the literature. We present field profiles for  $\lambda = 600$  nm to serve as a qualitative representative of optical profiles within each device. Surface parameters for Asahi substrates are imported from atomic force microscope (AFM) measurements. Further simulation details are described in Appendix B.

For nanovoid cells, increasing the spacer thickness changes the localized plasmon profile within the device. For thin spacer thickness [Fig. 5(a)], weak excitation of plasmon field is observed with the strongest localization found for an Al:ZnO thickness of 100 nm [Fig. 5(b)]. With 200 nm of Al:ZnO [Fig. 5(c)], the resonant field is again reduced in strength, qualitatively matching the response found in the photocurrent [Fig. 2(b)]. For each void geometry the field profile is strongly tethered to the surface and has only a weak overlap with the amorphous silicon layer. This is in contrast to the field profiles found previously for organic solar cells fabricated in silver

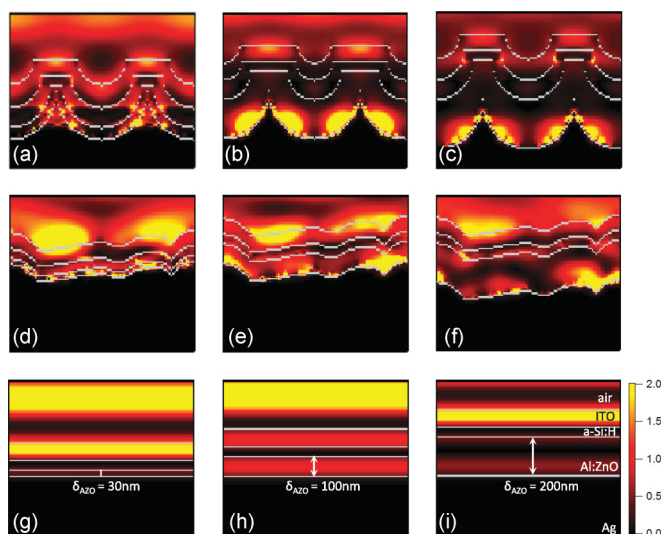


FIG. 5. (Color online) FDTD simulations of  $|E|^2$  intensity at 600 nm with increasing Al:ZnO spacer thicknesses of 30 100 and 200 nm (left to right) for (a-c) nanovoids, (d-f) Asahi, and (g-i) flat solar cells.

nanovoids<sup>4</sup> highlighting the strong material dependence on plasmon absorption enhancement via the near field, discussed further in Sec. V.

Contrasting these void plasmon optical fields are those found in the Asahi cells [Figs. 5(d)–5(f)] which retain strong field enhancements for each spacer layer. For 30-nm spacing, strong fields are observed across the Ag/Al:ZnO interface. For 200-nm spacing we see a more localized field at the metal interface, but also an increase of field inside the a-Si:H layer with optical nulls on either side in the lower- $n$  ITO and Al:ZnO layers [Fig. 5(f)]. This guided mode profile agrees with photocurrent measurements [Fig. 3(b)] and the strong field in the a-Si:H layer highlights the role of scattering when compared with the null observed in the a-Si:H layer for the flat cell with the same spacer thickness [Fig. 5(i)]. Field profiles for flat cells show minimal overlap with the a-Si:H layer at 600 nm, highlighting the need for scattering features to couple incoming light to guided modes within the higher- $n$  layer.

##### B. Spectral analysis

The effect of scattering features on absorption is observed through normal incidence extinction measurements (Fig. 6) of Asahi and flat cells. Peaks of absorption in Al:ZnO-coated flat silver broaden and redshift when deposited on the randomly

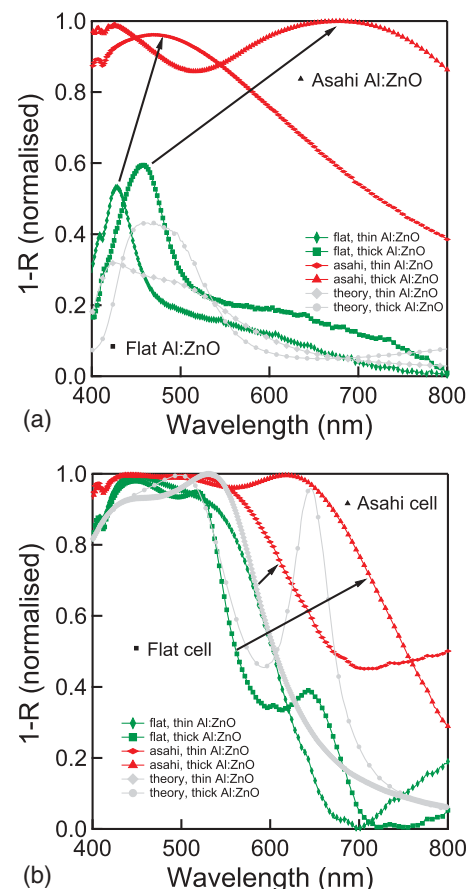


FIG. 6. (Color online) Extinction = (1 reflectance) spectra for flat and Asahi substrates coated with (a) Al:ZnO and (b) additional cell layers. Transfer matrix calculations (grey lines) show the position of Fabry-Perot peaks within planar substrates.

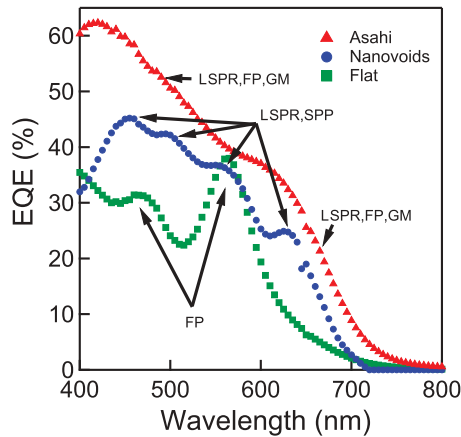


FIG. 7. (Color online) External quantum efficiency of a-Si solar cells fabricated on Asahi VU type glass, Nanovoids, and Flat silver substrates. LSPR = localized surface plasmon resonance, FP = Fabry-Perot resonance, GM = Guided mode.

textured substrate [Fig. 6(a)], showing the detuning of LSPRs. For the complete cell structure [Fig. 6(b)], both substrates retain a FP-type spectral profile with the Asahi substrate displaying both stronger and broader absorption. This is explained by the Asahi substrate providing scattering in multiple directions, allowing a broad range of optical paths within the device, and coupling to guided modes within the a-Si:H layer clad with the lower-*n* layers of ITO and Al:ZnO.

EQE spectra for solar cells with 200-nm Al:ZnO spacer layer (Fig. 7) reveal characteristics for each physical process. Scattering from localized plasmons and FP resonances which couple to guided modes result in enhanced optical path lengths within the device, contributing to an increased photocurrent across the spectrum for Asahi cells. The sharper localized plasmon resonances of nanovoid cells [Fig. 2(f)] are visible in the EQE spectrum, though little photocurrent is observed at either short (<450 nm) or longer (>600 nm) wavelengths. The dip in photocurrent below 450 nm alongside the weaker scattering from the more narrow surface plasmon polariton (SPP) peaks are the main cause of the reduced  $J_{sc}$  of the nanovoids compared to the Asahi cells. EQE spectra of the flat solar cell highlight the importance of matching FP modes spatially with the active absorbing layer for ultrathin devices. With the 50-nm thickness of the a-Si layer being much less than the absorption length (190 nm at  $\lambda = 600$  nm) and in the absence of in-plane coupling, photocurrent generation relies significantly on light-trapping within the active absorbing layer [Fig. 4(b)].

The dependence on scattering geometry is apparent when we compare the effect of spacer layer thickness for each device type (Fig. 8). With broad scattering resonances, randomly textured glass benefits monotonically from increased spacer layer thicknesses. The optimum thickness for this ultrathin device expected when decreasing charge collection due to the thick Al:ZnO layer counteracts the optical enhancement gained from enhanced scattering into guided modes. Nanovoid cells with strong narrow plasmon resonances generate absorption in the Ag for shorter wavelengths suppressing photocurrent for thin Al:ZnO thicknesses. Optimum photocurrent arises for 100 nm Al:ZnO when the spatial distribution of plasmon modes

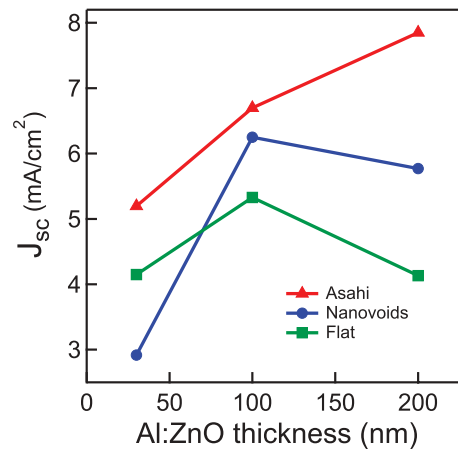


FIG. 8. (Color online) Short-circuit current density versus Al:ZnO thickness for each substrate.

overlaps best with the a-Si:H layer. For 200-nm spacers the narrow linewidths of the plasmon coupled modes now redshift below the region of strong a-Si absorption, resulting in reduced photocurrent from shorter wavelengths and lower  $J_{sc}$ . The effect of Al:ZnO thickness on flat cells is to shift the spatial intensity distribution across the device. For 100-nm thickness, an FP peak in the a-Si layer contributes most to give maximum  $J_{sc}$ .

### C. Geometry and curvature

To examine the dependence of geometry on the effect of the near-field plasmon resonance, we examine solar cells with thin Al:ZnO layers deposited on spherical nanovoids with radii of 100, 150, 200, and 250 nm (Fig. 9). The  $J_{sc}$  of each is plotted against the curvature of the voids ( $1/R$ ) with flat and Asahi provided for comparison. The curvature of silver-coated Asahi is obtained from AFM measurements of the RMS roughness. Nanovoid  $J_{sc}$  decreases with increasing curvature (decreasing radius) of the nanovoid. This is because as the radius of the nanovoid decreases, localized plasmon resonances are excited at higher energies<sup>30</sup> and are unable to generate enhanced photocurrent in the a-Si:H layer.

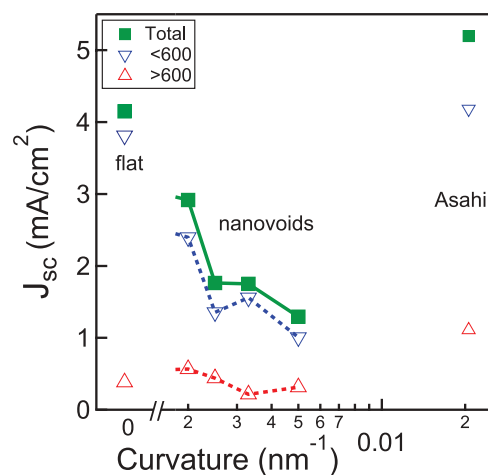


FIG. 9. (Color online)  $J_{sc}$  vs curvature for cells with 30 nm Al:ZnO on flat silver, nanovoids with radius 100, 150, 200, and 250 nm, and silver-coated Asahi glass.

The effect of plasmonic geometry is found to be significantly different for nanovoids and randomly textured silver, with the Asahi cells not matching the trend of reduced  $J_{sc}$  for increased curvature. This highlights a key optical difference between the confined localized plasmons of nanovoids and the plasmon-enhanced scattering of the Asahi substrate, with the scattering proving more beneficial for solar cells made with a-Si:H active layers.

## V. MATERIAL DEPENDENCE OF PLASMON ABSORPTION

To understand the differences in plasmonic enhancement between these amorphous silicon solar cells, previously fabricated organic solar cells, and plasmonic solar cells of various materials presented in the literature,<sup>1</sup> we analytically examine the balance of absorption from the intensity distribution of surface plasmon polaritons at a planar interface between silver and an absorbing semiconductor. This derivation allows us to understand when the plasmonic near field may be found to enhance absorption in an adjacent semiconductor, and when it can be expected to lead to undesired absorption in the metal layer. This is a question that has not yet been resolved satisfactorily in the literature.

By considering the expression for energy dissipation in a lossy medium  $P = \int d\mathbf{r} 2\omega\epsilon_0 \text{Im}(\tilde{\epsilon}_j) |\bar{E}|^2$  and the wave vectors for a surface plasmon traveling in the  $x$  direction at the interface between a metal ( $\tilde{\epsilon}_m, z \leq 0$ ) and absorbing dielectric ( $\tilde{\epsilon}_d, z > 0$ ), with wave vectors  $\tilde{k}_x = k_0 \sqrt{\frac{\tilde{\epsilon}_d \tilde{\epsilon}_m}{\tilde{\epsilon}_d + \tilde{\epsilon}_m}}$  and  $\tilde{k}_{z_j} = \sqrt{k_0^2 \tilde{\epsilon}_j - \tilde{k}_x^2}$ , with  $k_0 = \frac{\omega}{c}$ , we find the ratio of power absorbed in the dielectric to the metal given by

$$\frac{P_d}{P_m} = \frac{k_{z_m}^i \text{Im}(\tilde{\epsilon}_d)(1 + |\tilde{k}_x|^2/|\tilde{k}_{z_d}|^2)}{k_{z_d}^i \text{Im}(\tilde{\epsilon}_m)(1 + |\tilde{k}_x|^2/|\tilde{k}_{z_m}|^2)}, \quad (1)$$

where the superscript  $k^i$  indicates the imaginary part. This simple expression (with the derivation included in Appendix A) comprising only dielectric functions allows us to identify materials for which the plasmonic near field is expected to contribute beneficially to absorption enhancement in the semiconductor. For solar cells with plasmonic surfaces adjacent to the rear of the semiconductor layer, a high absorption ratio close to the band-gap edge is desired. Since light of shorter wavelengths is preferentially absorbed near the front surface, plasmonic surfaces at the rear of the cell should be optimally designed to increase absorption of light of longer wavelengths near the band-gap edge.<sup>37</sup> For cells made on Ag substrates we see that each of a-Si, GaAs, and c-Si ratios show decreasing semiconductor absorption for energies approaching their respective bandgaps (Fig. 10), crystalline silicon showing particularly strong parasitic metal absorption for much of the visible spectrum.

For ultrathin solar cells with thickness at or below the absorption depth even for short wavelengths, a high absorption ratio in the semiconductor is desired across the spectrum.

On the other hand, CdTe, CuInGaSe<sub>2</sub> (CIGS), and organic polymers are found to absorb more than 80% of the plasmonic near field across the spectrum (where a typical blend of P3HT:PCBM with band-gap edge at  $\sim 2$  eV is used for the organic polymer). These results enable us to predict the

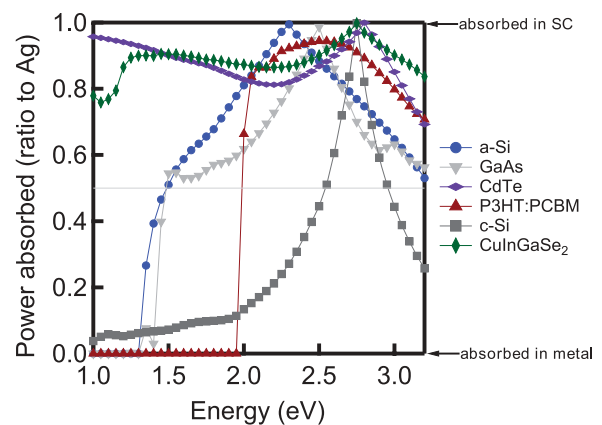


FIG. 10. (Color online) Ratio of power absorbed in semiconductor and metal for various semiconductors. A silver substrate with a surface plasmon polariton is excited at the interface.

materials for which plasmonic near-field excitation will be most beneficial to absorption enhancement (CdTe, CIGS, and organic polymers), and where plasmonic substrates should be harnessed more for increased scattering (a-Si, GaAs, and c-Si). These two mechanisms can be mediated via the thickness and refractive index of the spacer layer, with thin low- $n$  dielectrics suited for near-field coupling. For ultrathin active layers, thicker high- $n$  dielectrics are more suited to generate increased optical thickness that allows for enhanced scattering into guided modes. The balance for crystalline silicon indicates that structures should be as scattering as possible (e.g., nanoparticles, as examined by the authors of Ref. 18).

## VI. CONCLUSION

Ultrathin amorphous silicon solar cells are fabricated with varying Al:ZnO spacer layers on two different plasmonic substrates alongside flat silver as a reference. Angle-resolved reflectance and photocurrent measurements allow identification of the coupling mechanisms of light with varying spacer layer, highlighting the importance of separating the absorbing and plasmonic layers. The broad plasmonic resonances of silver-coated randomly textured glass benefit from larger optical thicknesses supporting enhanced scattering within the device leading to increased optical path lengths and 50% higher  $J_{sc}$  than for cells with thin spacer layers. The spacer layer in flat solar cells adjusts the spatial profile of the field intensity within the device, with the greatest absorption enhancement achieved when FP resonances peak within the active layer.

Classical analysis of power absorbed at the interface between a metal and a dielectric provides guidance for choosing the role of a plasmonic rear surface. For CdTe, CIGS, and organic polymers, the near field proves beneficial and the spacer layer is recommended to be a thin low- $n$  dielectric. For thin a-Si, GaAs, and c-Si cells, absorption in the metal substrate can be suppressed through the inclusion of a thicker high- $n$  dielectric as the spacer layer, allowing coupling of plasmonic scattering to guided modes within the active layer.

For ultrathin solar cells, controlling the Al:ZnO spacer thickness generates an increase in  $J_{sc}$  between 50–100% compared to solar cells with thin spacer layers. Spacer layers physically separate the semiconductor from the absorbing

metal, reducing the near-field coupling and allowing greater scattering into optical modes. For higher- $n$  semiconductor solar cells the device design considerations arising from this study are to use features with broad scattering resonances across the spectrum and to maximize the total optical thickness of the device, which can be achieved while retaining an ultrathin active layer. High- $n$  dielectric spacer layers such as  $\text{TiO}_2$  show significant promise for this.

Thin cells allow the use of less material, faster throughput, higher internal fields, and the use of novel active layers. To increase absorption within thin active layers, plasmonic structures have been intensively studied for both near-field enhancement and greater scattering into guided modes within the devices. Alongside the nature of plasmonic resonances, the thickness of the spacer layer is here identified to be a critical and useful parameter for device design.

### ACKNOWLEDGMENTS

The authors wish to thank F. J. Garcia de Abajo for helpful guidance with theoretical analysis. We acknowledge the UK Engineering and Physical Sciences Research Council (EPSRC) Grants No. EP/C511786/1, No. EP/F059396/1, and No. EP/E040241. NNL acknowledges the support of the Gates Cambridge Scholarship.

### APPENDIX A: DERIVATION OF THE ABSORPTION RATIO BETWEEN A SEMICONDUCTOR AND METAL WITH A SURFACE PLASMON FIELD EXCITED AT THE INTERFACE

Consider an electromagnetic wave at the  $z = 0$  plane, traveling in the  $x$  direction with the imaginary wave vector in the  $z$  direction. The general expression for the electric field is given as follows:

$$\vec{E} = (E_x, E_y, E_z) e^{i(\tilde{k}_x x + \tilde{k}_z z)} \quad (\text{A1})$$

with  $\text{Re}(k_x)$  and  $\text{Im}(k_z)$ . The dispersion relation for a surface plasmon polariton at a metal/dielectric interface yields expressions for the wave vectors

$$\tilde{k}_x = k_0 \sqrt{\frac{\tilde{\epsilon}_1 \tilde{\epsilon}_2}{\tilde{\epsilon}_1 + \tilde{\epsilon}_2}}, \quad (\text{A2})$$

$$\tilde{k}_z = \sqrt{k_0^2 \tilde{\epsilon}_j - \tilde{k}_x^2}, \quad (\text{A3})$$

where  $k_0$  is the wave vector for light in a vacuum  $\frac{\omega}{c}$ , and  $\tilde{k}_{z_j}$  is the  $z$  wave vector in each medium  $j$ . We then identify each component of the electric field

$$E_x = C_1 e^{i(\tilde{k}_x x + \tilde{k}_z z)}, \quad (\text{A4})$$

$$E_y = 0, \quad (\text{A5})$$

$$E_z = i C_1 \frac{\tilde{k}_x}{\tilde{k}_z} e^{i(\tilde{k}_x x + \tilde{k}_z z)}. \quad (\text{A6})$$

This allows calculation of the field intensity

$$|\vec{E}|^2 = (\vec{E} \cdot \vec{E}^*) \quad (\text{A7})$$

$$= C_1^2 \left( 1 + \frac{|\tilde{k}_x|^2}{|\tilde{k}_{z_j}|^2} \right) e^{-2\text{Im}(\tilde{k}_{z_j})z}. \quad (\text{A8})$$

By considering the expression for energy dissipation in a lossy medium  $P = \int d\mathbf{r} 2\omega\epsilon_0 \text{Im}(\tilde{\epsilon}_j) |\vec{E}|^2$  we can form the integral for power absorbed as a function of height

$$P = \int d\mathbf{r} 2\omega\epsilon_0 \text{Im}(\tilde{\epsilon}_j) \left( 1 + \frac{|\tilde{k}_x|^2}{|\tilde{k}_{z_j}|^2} \right) e^{-2\text{Im}(\tilde{k}_{z_j})z}. \quad (\text{A9})$$

Integrating in the half-plane then yields the expression for plasmon absorption for each material

$$P = \frac{\omega}{k_{z_1}^i} \epsilon_0 \text{Im}(\tilde{\epsilon}_1) \left( 1 + \frac{|\tilde{k}_x|^2}{|\tilde{k}_{z_1}|^2} \right). \quad (\text{A10})$$

From which we obtain the ratio of absorption in a dielectric ( $d$ ) to the metal ( $m$ )

$$\frac{P_d}{P_m} = \frac{k_{z_m}^i \text{Im}(\tilde{\epsilon}_d) (1 + |\tilde{k}_x|^2 / |\tilde{k}_{z_d}|^2)}{k_{z_d}^i \text{Im}(\tilde{\epsilon}_m) (1 + |\tilde{k}_x|^2 / |\tilde{k}_{z_m}|^2)}. \quad (\text{A11})$$

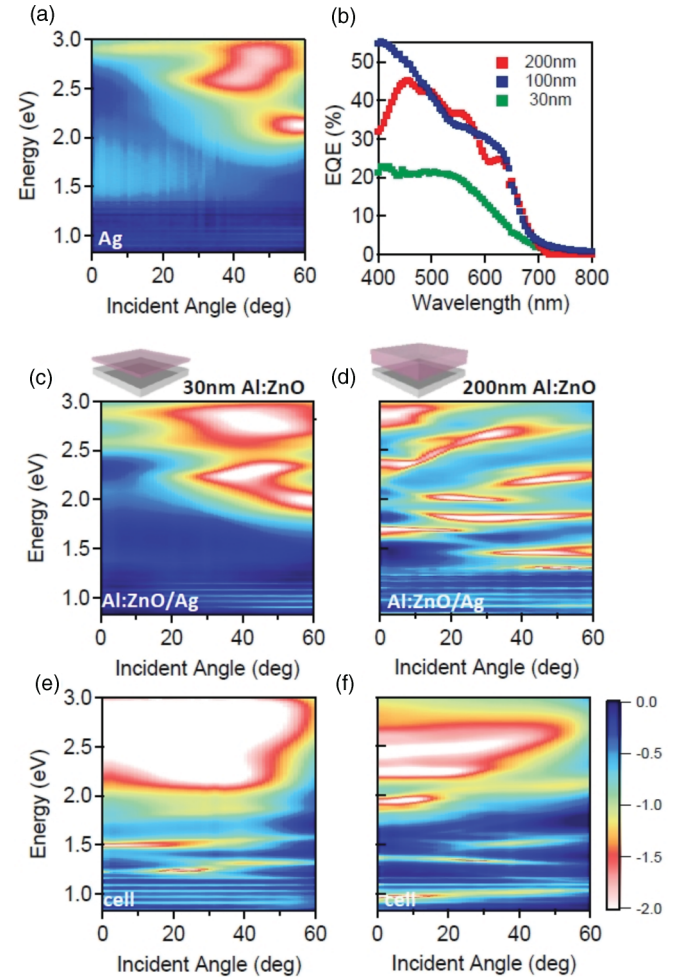


FIG. 11. (Color online) Angle reflectance scans in TE of silver nanovoids (a) uncoated, (c, d) coated with Al:ZnO of 30 and 200 nm, and (e, f) complete solar cells as indicated. Color scale is  $\log(\text{reflectance})$  with blue indicating high reflectance and red-white indicating low reflectance. (b) EQE for nanovoids cells with varying Al:ZnO thickness.

**APPENDIX B: MODELING INFORMATION**

Finite difference time-domain simulations are undertaken with Lumerical FDTD Solutions software. Illumination is via a plane wave at normal incidence. The simulated region is  $2 \mu m^2$  in area, boundary conditions are perfectly matched layers in the  $z$  direction and periodic in  $x, y$ . With illumination at normal incidence and with reference to previous modeling (Ref. 24) the errors arising from periodic boundary conditions for the randomly textured cell are expected to be  $<5\%$ . The randomly textured silver profile is imported from AFM measurements.

**APPENDIX C: SUPPLEMENTARY FIGURES**

Supplementary figures of EQE and angle-resolved reflectance with TE illumination for nanovoids (Fig. 11), randomly textured silver (Fig. 12), and flat silver (Fig. 13).

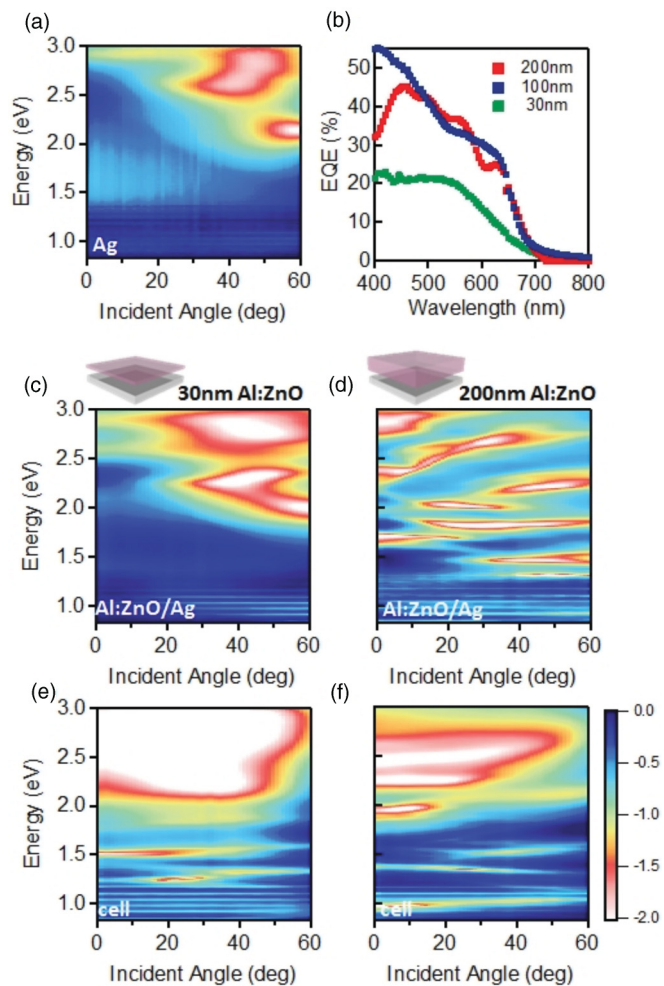


FIG. 12. (Color online) Angle reflectance scans in TE of (a) silver-coated Asahi glass, (c, d) coated with Al:ZnO of 30 and 200 nm, (e, f) and complete solar cells as indicated. Color scale is  $\log(\text{reflectance})$  with blue indicating high reflectance and red-white indicating low reflectance. (b) EQE for Asahi cells with varying Al:ZnO thickness.

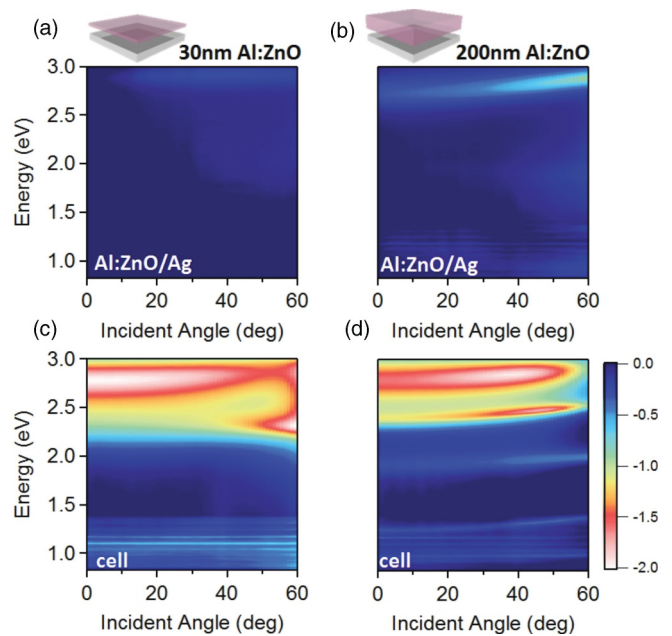


FIG. 13. (Color online) Angle reflectance scans in TE of flat silver (a) uncoated, (c, d) coated with Al:ZnO of 30 and 200 nm, (e, f) and complete solar cells as indicated. Color scale is  $\log(\text{reflectance})$  with blue indicating high reflectance and red-white indicating low reflectance. (b) EQE for flat cells with varying Al:ZnO thickness.

Figure 14 presents EQE for nanovoids of varying radius, alongside flat and randomly textured silver each with 30 nm coating of Al:ZnO. Angled reflectance of voids with varying radius (Fig. 15) presents the evolution of plasmon excitation towards higher energies with decreasing void radius.

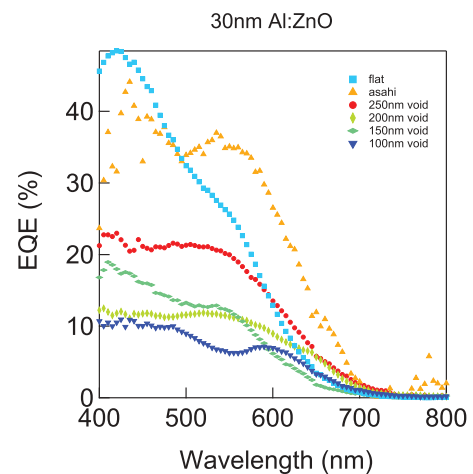


FIG. 14. (Color online) External quantum efficiency versus wavelength for solar cells with 30 nm coating of Al:ZnO and varying substrate geometry.

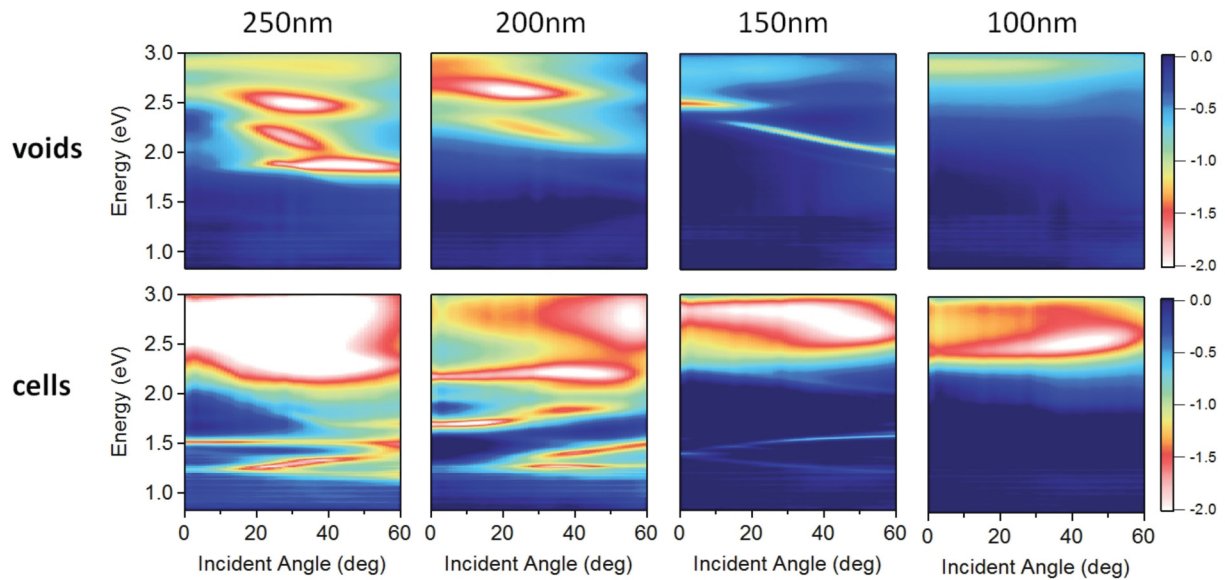


FIG. 15. (Color online) Angle reflectance (TM) scans of nanovoids with varying radius coated with 30 nm of Al:ZnO (top) and complete solar cell layers (bottom). Left to right 250, 200, 150, and 100 nm.

- <sup>1</sup>H. A. Atwater and A. Polman, *Nat. Mater.* **9**, 205 (2010).
- <sup>2</sup>K. R. Catchpole and A. Polman, *Opt. Express* **16**, 21793 (2008).
- <sup>3</sup>S. Pillai, K. R. Catchpole, T. Trupke, and M. A. Green, *J. Appl. Phys.* **101**, 093105 (2007).
- <sup>4</sup>N. N. Lal *et al.*, *Opt. Express* **19**, 3918 (2011).
- <sup>5</sup>J. W. Menezes *et al.*, *Adv. Funct. Mater.* **20**, 3918 (2010).
- <sup>6</sup>V. E. Ferry *et al.*, *Appl. Phys. Lett.* **95**, 183503 (2009).
- <sup>7</sup>R. B. Dunbar, H. C. Hesse, D. S. Lembke, and L. Schmidt-Mende, *Phys. Rev. B* **85**, 035301 (2012).
- <sup>8</sup>A. Krishnan *et al.*, *Opt. Commun.* **200**, 1 (2001).
- <sup>9</sup>Z. H. Tang, R. W. Peng, Z. Wang, X. Wu, Y. J. Bao, Q. J. Wang, Z. J. Zhang, W. H. Sun, and M. Wang, *Phys. Rev. B* **76**, 195405 (2007).
- <sup>10</sup>Y. J. Bao, R. W. Peng, D. J. Shu, M. Wang, X. Lu, J. Shao, W. Lu, and N. B. Ming, *Phys. Rev. Lett.* **101**, 087401 (2008).
- <sup>11</sup>K. Tvingstedt *et al.*, *Appl. Phys. Lett.* **91**, 113514 (2007).
- <sup>12</sup>V. E. Ferry, L. A. Sweatlock, D. Pacifici, and H. A. Atwater, *Nano Lett.* **8**, 4391 (2008).
- <sup>13</sup>R. A. Pala *et al.*, *Adv. Mater.* **21**, 3504 (2009).
- <sup>14</sup>V. E. Ferry, A. Polman, and H. A. Atwater, *ACS Nano* **5**, 10055 (2011).
- <sup>15</sup>V. E. Ferry *et al.*, *Nano Lett.* **11**, 4239 (2011).
- <sup>16</sup>J. Zhu *et al.*, *Nano Lett.* **10**, 1979 (2010).
- <sup>17</sup>M. Green and S. Pillai, *Nature Photonics* **6**, 130 (2012).
- <sup>18</sup>S. Pillai *et al.*, *J. Appl. Phys.* **109**, 073105 (2011).
- <sup>19</sup>F. J. Beck *et al.*, *Opt. Express* **19**, A146 (2011).
- <sup>20</sup>S. Standridge, G. Schatz, and J. Hupp, *J. Am. Chem. Soc.* **131**, 8407 (2009).
- <sup>21</sup>C. Hagglund and S. P. Apell, *J. Phys. Chem. Lett.* **3**, 1275 (2012).
- <sup>22</sup>F. J. Haug *et al.*, *J. Appl. Phys.* **104**, 064509 (2008).
- <sup>23</sup>F. J. Haug *et al.*, *J. Appl. Phys.* **106**, 044502 (2009).
- <sup>24</sup>V. E. Ferry, A. Polman, and H. A. Atwater, *ACS Nano* **5**, 10055 (2011).
- <sup>25</sup>A. Lin and J. Phillips, *Solar Energy Materials and Solar Cells* **92**, 1689 (2008).
- <sup>26</sup>W. Ren *et al.*, *Opt. Express* **19**, 26536 (2011).
- <sup>27</sup>C. Kothandaraman, T. Tonon, C. Huang, and A. Delahoy, *Materials Research Society Symposium* **219**, 475 (1991).
- <sup>28</sup>Asahi Co. Ltd. [[www.agc.com](http://www.agc.com)].
- <sup>29</sup>T. A. Kelf, Y. Sugawara, R. M. Cole, J. J. Baumberg, M. E. Abdelsalam, S. Cintra, S. Mahajan, A. E. Russell, and P. N. Bartlett, *Phys. Rev. B* **74**, 245415 (2006).
- <sup>30</sup>R. M. Cole *et al.*, *Nano Lett.* **7**, 2094 (2007).
- <sup>31</sup>C. Battaglia *et al.*, *ACS Nano* **6**, 2790 (2012).
- <sup>32</sup>M. A. Green, *Progress in Photovoltaics: Research and Applications* **19**, 473 (2011).
- <sup>33</sup>Lumerical FDTD Solutions Inc. (2012).
- <sup>34</sup>G. Palik and E. Ghosh, *Handbook of Optical Constants of Solids*, 3 ed. (Academic Press, New York, 1998).
- <sup>35</sup>M. Caglar, S. Ilican, Y. Caglar, and F. Yakuphanoglu, *J. Mater. Sci.: Mater. Electron.* **19**, 704 (2007).
- <sup>36</sup>Sopra nk Database [[www.sopra-sa.com](http://www.sopra-sa.com)].
- <sup>37</sup>F. J. Beck, S. Mokkaapati, A. Polman, and K. R. Catchpole, *Appl. Phys. Lett.* **96**, 033113 (2010).